Suspension Force Modeling for a Bearingless Permanent Magnet Synchronous Motor Using Maxwell Stress Tensor Method

Xiaodong Sun, *Member, IEEE*, Zhengwang Xue, Jianguo Zhu, *Senior Member*,
Youguang Guo, *Senior Member*, Zebin Yang, Long Chen, and Jianfeng Chen

***Abstract*—Bearingless permanent magnet synchronous motors (BPMSMs) have been received more and more attention during the past few decades. To realize the high-performance control for rotation and levitation, we will first need to obtain the accurate suspension force model of a BPMSM. In this work, different from conventional suspension force models, a modeling scheme for the suspension force of a BPMSM is presented by taking into account rotor eccentricity with the Maxwell stress tensor modeling scheme. The theoretical value of suspension force model is compared by the two-dimensional finite element (FE) analysis, and calculation results reveal that the theoretical value closely agree with the FE computed one. Furthermore, the digital control system is devised by taking advantage of TMS320F2812, and a test platform for experiments is then set up. In accordance with the corresponding findings of the experiments, the rotor stabilization with magnetic levitation can be achieved. The results lay a theoretical and experimental foundation for further study of the BPMSM.**

***Index Terms*—Bearingless motor, finite element, modeling, permanent magnet synchronous motor, suspension force.**

I. INTRODUCTION

THE PERMANENT magnet (PM) motor has caused widespread concern in academia [1]-[4], because of its merits including the high efficiency, high reliability, high-speed capacity, and high power density. However, the increase of the PM motor speed will lead to the increase of the friction between the motor shaft and bearings, which influences the bearing lifespan and system reliability. Therefore, in order to overcome the shortcoming above, the high speed PM motors and magnetic bearings [5] with the up-to-date materials [6], [7] have been widely used in the last decade. An alternative solution is to combine the bearingless machine technology with the PM motors to provide both functions: torque and levitation force, in the same machine [8]-[11]. Fig. 1 illustrates the term meaning *bearingless*: the electromagnetic torque and suspension forces can be produced in a single device, which significantly reduces the axial space. Among various kinds of bearingless PM motors, the bearingless PM synchronous motors (BPMSMs) are arousing more and more interest in recent years since they have outstanding merits including simple structure, high operation reliability, as well as mature classical control technologies [12]-[15].

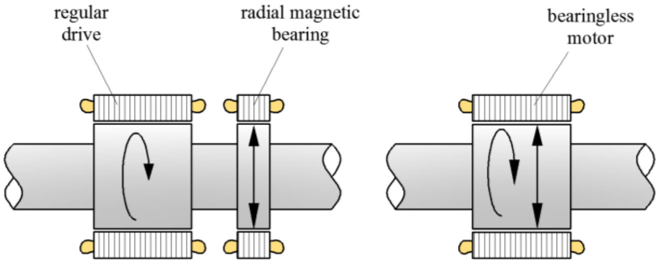

Fig. 1. Meaning of term *bearingless motors*.

To obtain the satisfactory control performances of suspension and rotation of BPMSMs, it is especially significant to set up an accurate suspension force model of a BPMSM [16], [17]. Usually, the suspension force model of the BPMSM is acquired on condition that the rotor is not eccentric. But actually, the rotor eccentricity is inevitable since there are measurement errors during the machine installation, as well as the load disturbances in rotation and levitation [18]. The aim of this work is to present a modeling scheme for suspension force of a BPMSM using Maxwell tensor approach on condition that the rotor is eccentric. In Section II, the suspension force model will be deduced using Maxwell tensor method. In Section III, the simulation study about comparison of finite element (FE) computed value and the theoretical value will be analyzed. In Section IV, the experimental study will be carried out. Finally, conclusion will be drawn in Section IV.

Manuscript received February 26, 2016; accepted August 08, 2016. This work was supported in part by the National Natural Science Foundation of China under Projects 51305170, U1564201, 51475214, and 51405203, by the National Science Foundation of Jiangsu Province under Projects BK20130515, and BK20141301, by the China Postdoctoral Science Foundation under Project 2015T80508, by the Six Categories Talent Peak of Jiangsu Province under Projects 2015-XNYQC-003 and 2014-ZBZZ-017, and by the Priority Academic Program Development of Jiangsu Higher Education Institutions (PAPD).

X. Sun, Z. Xue, L. Chen, and J. Chen are with the School of Automobile and Traffic Engineering, and the Automotive Engineering Research Institute, Jiangsu University, Zhenjiang 212013, China (e-mail: xdsun@ujs.edu.cn; xzw901008@163.com; chenlong@ujs.edu.cn; cjf@ujs.edu.cn).

J. Zhu and Y. Guo are with the School of Electrical, Mechanical and Mechatronic Systems, University of Technology Sydney, Sydney, N.S.W. 2007, Australia (e-mail: jianguo.zhu@uts.edu.au; Youguang.Guo-1@uts.edu.au).

Z. Yang is with the School of Electrical and Information Engineering, Jiangsu University, Zhenjiang 212013, China (e-mail: zbyang@ujs.edu.cn).

II. MATHEMATICAL MODEL OF THE SUSPENSION FORCE

The Maxwell force components F_{n} and F_{t} of the BPMSM can be given as:

$$\begin{cases} \mathrm{d}F_{\mathrm{n}} = \dfrac{b_{\mathrm{n}}^2(\theta,t)}{2\mu_0}\mathrm{d}S = \dfrac{b_{\mathrm{n}}^2(\theta,t)}{2\mu_0}\cdot(lr\mathrm{d}\theta) \\ \mathrm{d}F_{\mathrm{t}} = \dfrac{b_{\mathrm{n}}(\theta,t)\cdot b_{\mathrm{t}}(\theta,t)}{\mu_0}\mathrm{d}S = \dfrac{b_{\mathrm{n}}(\theta,t)\cdot b_{\mathrm{t}}(\theta,t)}{\mu_0}\cdot(lr\mathrm{d}\theta) \end{cases} \tag{2}$$

where $b_{\mathrm{n}}(\theta, t)$ is the normal component of airgap flux density, $b_{\mathrm{t}}(\theta, t)$ is the tangential component, μ_0 is the vacuum magnetic permeability, dS is unit area, θ is the mechanical angle, r and l are respectively the outer radius and equivalent length of the rotor.

Then, we can get the suspension force expression:

$$\begin{cases} \mathrm{d}F_{\alpha}(\theta) = \left[\dfrac{b_{\mathrm{n}}(\theta,t)^2}{2\mu_0}lr\cos\theta + \dfrac{b_{\mathrm{n}}(\theta,t)\cdot b_{\mathrm{t}}(\theta,t)}{\mu_0}lr\sin\theta\right]\mathrm{d}\theta \\ \mathrm{d}F_{\beta}(\theta) = \left[\dfrac{b_{\mathrm{n}}(\theta,t)^2}{2\mu_0}lr\sin\theta + \dfrac{b_{\mathrm{n}}(\theta,t)\cdot b_{\mathrm{t}}(\theta,t)}{\mu_0}lr\cos\theta\right]\mathrm{d}\theta \end{cases} \tag{3}$$

where F_{α} and F_{β} are horizontal and vertical components in α- and β- directions.

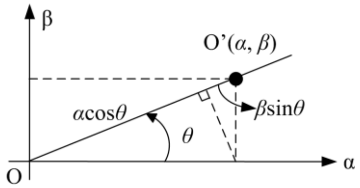

Fig. 2. Diagram of rotor eccentricity.

Fig. 2 shows the diagram of rotor eccentricity, where O(0, 0) and O'(α, β) are the coordinate of the axle centre without rotor eccentricity and coordinate of the axle centre when the rotor is eccentric, respectively. The eccentric angle θ can be expressed as:

$$\theta = \arctan(\beta/\alpha) \tag{4}$$

where α and β are radial displacements of the rotor in α- axis and β- axis. The airgap length $g(\theta)$ can be given as:

$$g(\theta) = g_0 - (\alpha\cos\theta + \beta\sin\theta) \tag{5}$$

where g_0 is the uniform airgap length without rotor eccentricity.

Then, we can obtain the distribution function of the airgap permeance per unit area, and its expression can be given as

$$\Lambda(\theta) = \frac{\mu_0}{g(\theta)} \approx \frac{\mu_0}{g_0^{\,2}}(g_0 + \alpha\cos\theta + \beta\sin\theta) \tag{6}$$

where $\Lambda(\theta)$ is the airgap permeance. If the higher harmonic components are neglected, we can obtain the fundamental components of magnetomotive force in the airgap:

$$\begin{cases} f_{\mathrm{M}}(\theta,t) = F_{\mathrm{M}}\cos(\omega t - P_{\mathrm{M}}\theta - \gamma_{\mathrm{M}}) \\ f_{\mathrm{B}}(\theta,t) = F_{\mathrm{B}}\cos(\omega t - P_{\mathrm{B}}\theta - \gamma_{\mathrm{B}}) \end{cases} \tag{7}$$

where $f_{\mathrm{M}}(\theta, t)$ and $f_{\mathrm{B}}(\theta, t)$ are the fundamental component of torque and suspension windings magnetomotive force in the airgap, respectively. F_{M} and F_{B} are the amplitudes of $f_{\mathrm{M}}(\theta, t)$ and $f_{\mathrm{B}}(\theta, t)$, respectively. γ_{M} and γ_{B} are the phase angles of airgap magnetomotive force in the two sets winding, respectively. ω is the electrical angle velocity of currents. When the rotor is eccentric, the torque and suspension windings magnetic flux density $b_{\mathrm{M}}(\theta, t)$ and $b_{\mathrm{B}}(\theta, t)$, as well as the amplitudes of magnetic flux density B_{M} and B_{B}, can be given as:

$$\begin{cases} b_{\mathrm{M}}(\theta,t) = \Lambda(\theta)\cdot f_{\mathrm{M}}(\theta,t) \\ b_{\mathrm{B}}(\theta,t) = \Lambda(\theta)\cdot f_{\mathrm{B}}(\theta,t) \end{cases} \tag{8}$$

$$\begin{cases} B_{\mathrm{M}} = \dfrac{\mu_0}{g_0}F_{\mathrm{M}} = \dfrac{\mu_0}{g_0}\left(\dfrac{3}{2}\cdot\dfrac{4}{\pi}\cdot\dfrac{1}{2}\cdot\dfrac{N_{\mathrm{M}}I_{\mathrm{M}}}{P_{\mathrm{M}}}\right) \\ B_{\mathrm{B}} = \dfrac{\mu_0}{g_0}F_{\mathrm{B}} = \dfrac{\mu_0}{g_0}\left(\dfrac{3}{2}\cdot\dfrac{4}{\pi}\cdot\dfrac{1}{2}\cdot\dfrac{N_{\mathrm{B}}I_{\mathrm{B}}}{P_{\mathrm{B}}}\right) \end{cases} \tag{9}$$

where N_{M} and N_{B} are respectively the single-phase effective turns of the torque winding and suspension winding; I_{M} and I_{B} are respectively the amplitudes of the torque winding current and suspension winding current. Thus, we can get the normal component of the synthetic gasgap flux density $b_{\mathrm{n}}(\theta, t)$

$$b_{\mathrm{n}}(\theta,t) = b_{\mathrm{M}}(\theta,t) + b_{\mathrm{B}}(\theta,t) \tag{10}$$

By computing the integral of (3), we can obtain F_{α} and F_{β}:

$$\begin{cases} F_{\alpha} \approx \dfrac{\pi lr}{2\mu_0}\left[B_{\mathrm{M}}B_{\mathrm{B}}\cos(\gamma_{\mathrm{M}} - \gamma_{\mathrm{B}}) + \dfrac{\alpha B_{\mathrm{M}}^2}{g_0}\right] + \dfrac{\pi lr\beta B_{\mathrm{t}}}{2\mu_0 g_0}B_{\mathrm{M}} \\ F_{\beta} \approx \dfrac{\pi lr}{2\mu_0}\left[B_{\mathrm{M}}B_{\mathrm{B}}\cos(\gamma_{\mathrm{M}} - \gamma_{\mathrm{B}}) + \dfrac{\beta B_{\mathrm{M}}^2}{g_0}\right] + \dfrac{\pi lr\alpha B_{\mathrm{t}}}{2\mu_0 g_0}B_{\mathrm{M}} \end{cases} \tag{11}$$

Moreover, the single-phase airgap flux linkage ψ_{M} of the torque winding are:

$$\psi_{\mathrm{M}} = \phi_{\mathrm{M}}N_{\mathrm{M}} = \frac{2lrB_{\mathrm{M}}}{P_{\mathrm{M}}}N_{\mathrm{M}} \tag{12}$$

where ϕ_{M} is the single-phase magnetic flux of torque winding. In addition, ψ_{M} can also be written as product of the mutual inductance L_{M} and current amplitude I_{M} of the torque winding.

$$\psi_{\mathrm{M}} = L_{\mathrm{M}}I_{\mathrm{M}} \tag{13}$$

Thus, we can rewrite (11) as:

$$\begin{cases} F_{\alpha} \approx k_1\psi_{\mathrm{M}}I_{\mathrm{B}}\cos(\gamma_{\mathrm{M}} - \gamma_{\mathrm{B}}) + k_2\alpha\psi_{\mathrm{M}}^2 + k_3\beta\psi_{\mathrm{M}} \\ F_{\beta} \approx k_1\psi_{\mathrm{M}}I_{\mathrm{B}}\sin(\gamma_{\mathrm{M}} - \gamma_{\mathrm{B}}) + k_2\beta\psi_{\mathrm{M}}^2 + k_3\alpha\psi_{\mathrm{M}} \end{cases} \tag{14}$$

where $k_1 = \dfrac{9\mu_0 lrN_{\mathrm{M}}N_{\mathrm{B}}}{4\pi g_0^2 L_{\mathrm{M}}}$, $k_2 = \dfrac{9\mu_0 lrN_{\mathrm{M}}^2}{8\pi g_0^3 L_{\mathrm{M}}^2}$, and $k_3 = \dfrac{3lrN_{\mathrm{M}}B_{\mathrm{t}}}{4\pi g_0^2 L_{\mathrm{M}}}$. According to (14), it is obvious that the suspension force consists of three parts: 1) As for the first part suspension force, it is the controllable suspension force acquired on condition that the rotor is not eccentric. By regulating the current of the suspension winding, we can change the magnetic field distribution in the airgap to control the controllable suspension force. 2) With regard to the second part suspension force, it is the unilateral magnetic force which will be produced when the rotor is eccentric. 3) Regarding the third part suspension force, it will be generated when the uneven distribution of the airgap flux density along the airgap circle in the rotor tangential surface is occurred.

III. SIMULATION STUDY

In this section, in accordance with the deduced suspension force model, the suspension force of the BPMSM is computed by the means of the finite element (FE) approach.

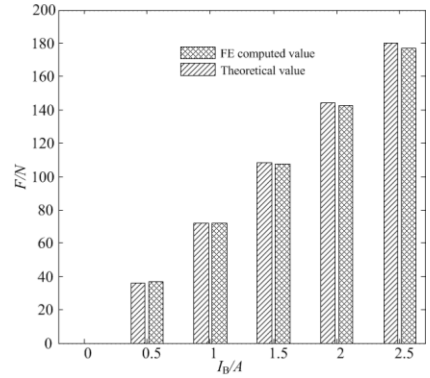

Fig. 3. Relationship between suspension force and suspension winding current with no rotor eccentricity.

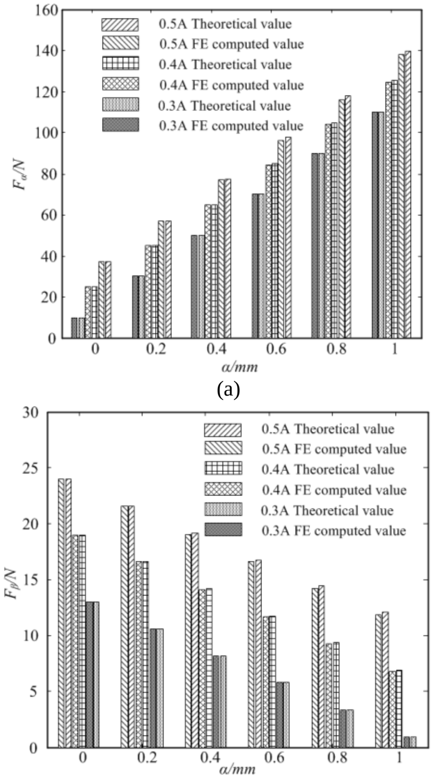

(a)

(b)

Fig. 4. Relationship between suspension force and eccentric displacements. (a) Suspension force components F_α. (b) Suspension force components F_β

Fig. 3 compares the FE computed value and the theoretical value of relationship between suspension force and the suspension winding current. In Fig. 3, the current of the torque winding is 1 A, and there is no rotor eccentricity. According to Fig. 3, it can be seen that the FE computed and theoretical values of suspension force is proportional to the suspension winding current. In addition, when the current of the suspension winding is approximately less than 2 A (i.e., the magnetic circuit is not saturated), the theoretical value of the suspension force is close to the FE computed value. Nevertheless, when the current of the suspension winding is approximately bigger than 2 A (i.e., the magnetic circuit is saturated), the FE computed value of the suspension force is a little bit small than the theoretical value.

Fig. 4 compares the FE computed value and the theoretical value of relationship between suspension force components and rotor eccentric displacement in α- axis. In Fig. 4, the current of the torque winding is 1 A, and the current of the suspension winding increases from 0.3 A to 0.5 A. As shown in Fig. 4, when the current of the suspension winding is also fixed, the FE computed and theoretical values of suspension force components F_α and F_β are proportional to the rotor eccentricity. Furthermore, when the change of the rotor eccentricity is the same, the bigger the current of the suspension winding, the bigger the suspension force components F_α and F_β. Moreover, when the values of the current of the suspension winding and rotor eccentricity are small (i.e., the magnetic circuit is not saturated), the theoretical value of the suspension force components F_α and F_β closely agree with the FE computed value. Nevertheless, the values of the current of the suspension winding and rotor eccentricity are bigger (i.e., the magnetic circuit is saturated), the FE computed value of the suspension force has a little deviation with the theoretical value. In addition, compared with Fig. 4(a) and (b), it is obvious that the influence of the rotor eccentricity in α- axis on suspension force component F_α is bigger than that on suspension force component F_β. In the same way, we can draw a conclusion that the varation of the rotor eccentricity in β- axis may primarily affect the suspension force component F_β.

IV. EXPERIMENT STUDY

The experimental studies are also implemented to further validate the effectiveness of the presented modeling scheme. The physical pictures of the BPMSM, including end view, wiring diagram, and interior view, are shown in Fig. 5. In the experimental studies, the digital control is carried on the Texas Instruments Incorporated digital signal processor (DSP) chip TMS320F2812. The DSP chip uses float-point arithmetic and its instruction execution speed is 150 MIPS. The sampling frequency is 6.67 kHz and the PWM control cycle is clocked with 20 kHz. The analog low-pass filters are used firstly to filter all the measured signals including the torque and suspension winding currents, rotor angle and position, and radial displacements, and then analog-to-digital converters (ADCs) of DSP are utilized to digitalize all these measured signals. With regard to current measurements of the two sets of windings, the Hall sensors are used to sample the current signals. As for the measurements of the rotor angle and position, an incremental photoelectric coded disk is chosen and employed. Regarding the measurements of the radial displacements, four eddy current displacement sensors are employed for two channels in α– and β- directions. Thus, two eddy current displacement sensors used in a channel are differential inputs to radial displacement interface circuits. Finally, after DSP completing the proposed control algorithm, the output signals of the DSP chip TMS320F2812 are pulse width modulation (PWM) signals for a three-phase inverter board.

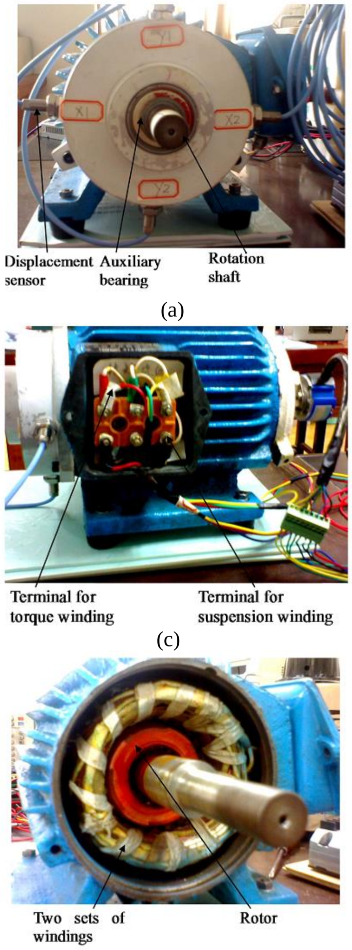

(a)

(c)

(b)

Fig. 5. Physical picture of experimental test. (a) End view. (b) Wiring diagram. (c) Interior view.

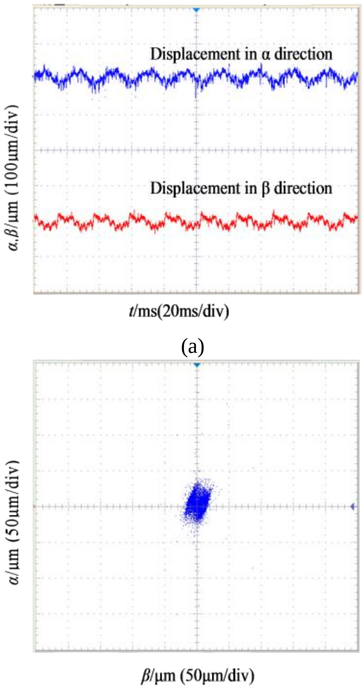

(a)

(b)

Fig. 6. Experimental results considering rotor eccentricity. (a) Rotor radial displacement. (b) Radial displacement relationship.

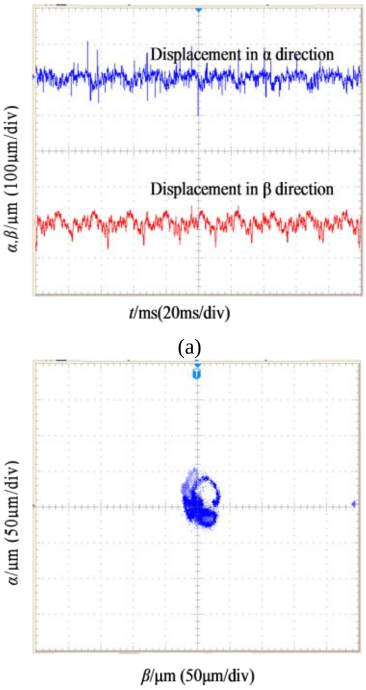

(a)

(b)

Fig. 7. Experimental results without considering rotor eccentricity. (a) Rotor radial displacement. (b) Radial displacement relationship.

Figs. 6 and 7 show comparison results of experimental studies (with speed 3000 r/min) when considering rotor eccentricity and without considering rotor eccentricity, respectively. Figs 6(a) and 7(a) are the displacement waveforms both in α– and β- directions, and Figs 6(b) and 7(b) are the trajectory of center of mass, respectively. According to Figs 6, it is obvious that when considering the rotor eccentricity, the rotor vibration amplitude in the in α– or β- direction is ±40 μm, as well as the peak- peak value of the rotor vibration amplitude is 80μm. On the other hand, from Fig. 7, we can see that without considering rotor eccentricity, the rotor vibration amplitude in the in α– or β- direction and the peak- peak amplitude value of the rotor vibration are ±50 μm and 100 μm, respectively. Therefore, according to Figs. 6 and 7, we can draw a conclusion that, when considering the rotor eccentricity, the control precision of radial displacement for the BPMSM can be increased by 20%.

V. CONCLUSION

In this paper, by taking into account the rotor eccentricity, a modeling scheme for the suspension force of a surface mounted BPMSM is presented using the Maxwell stress tensor method. Based on the FE method, a series of comparisons between the FE computed and theoretical values are conducted, and the results indicate that the theoretical value closely agrees with FE computed one. Additionally, the digital control system is designed based on TMS320F2812 chip, and corresponding experimental studies are carried out. On the basis of the findings of the experiments, the BPMSM can be levitated steadily with high control precision by the proposed modeling method.

REFERENCES

[1] G. Lei, T. Wang, J. Zhu, Y. Guo, and S. Wang, “System-level design optimization method for electrical drive systems-robust approach,” *IEEE Trans. Ind. Electron.*, vol. 62, no. 8, pp. 4702-4713, Aug. 2015.

[2] Y. Guo, J. Zhu, P. A. Watterson, and W. Wu, "Development of a PM transverse flux motor with soft magnetic composite core," *IEEE Trans. Energy Convers.*, vol. 21, pp. 426-434, Jue. 2006.

[3] G. Lei, C. Liu, J. Zhu, and Y. Guo, “Techniques for multilevel design optimization of permanent magnet motors,” *IEEE Trans. Energy Convers.*, vol. 30, no. 4, pp. 1574-1584, Dec. 2015.

[4] L. Chen, X. Sun, H. Jiang, and X. Xu, “High performance control of a permanent magnet synchronous motor for electric vehicle applications,” *J. Comput. Theor. Nanosci.*, vol. 11, no. 3, pp. 706-710, Mar. 2014.

[5] Z. Yu, G. Zhang, Q. Qiu, L. Hu, B. Zhuang, and M. Qiu, "Analyses and tests of HTS bearing for flywheel energy system," *IEEE Trans. Appl. Supercond.*, vol. 24, no. 3, Jun. 2014, Art. ID. 5700405.

[6] N. Duan, W. Xu, S. Wang, J. Zhu, and Y. Guo, “An improved XFEM with multiple high-order enrichment functions and low-order meshing elements for field analysis of electromagnetic devices with multiple nearby geometrical interfaces,” *IEEE Trans. Magn.*, vol. 51, no. 3, Mar. 2015, Art. ID. 7206004.

[7] N. Duan, W. Xu, S. Wang, J. Zhu, and Y. Guo, “Hysteresis modeling of high-temperature superconductor using simplified Preisach model,” *IEEE Trans. Magn.*, vol. 51, no. 3, Mar. 2015, Art. ID. 7300904.

[8] X. Sun, L. Chen, Z. Yang, and H. Zhu, “Speed-sensorless vector control of a bearingless induction motor with artificial neural network inverse speed observer,” *IEEE/ASME Trans. Mechatronics*, vol. 18, no. 4, pp. 1357-1366, Aug. 2013.

[9] X. Sun, L. Chen and Z. Yang, “Overview of bearingless permanent-magnet synchronous motors,” *IEEE Trans. Ind. Electron.*, vol. 60, no. 12, pp. 5528-5538, Dec. 2013.

[10] W. Bu, C. Lu, C. Zu, H. Zhang, and J. Xiao, "Inverse system decoupling control strategy of BLIM based on stator flux orientation," *Int. J. Appl. Electromagn. Mech.*, vol. 48, no. 4, pp. 469-480, Mar. 2015.

[11] X. Sun, L. Chen, H. Jiang, Z. Yang, J. Chen, and W. Zhang, “High-performance control for a bearingless permanent magnet synchronous motor using neural network inverse scheme plus internal model controllers,” *IEEE Trans. Ind. Electron.*, vol. 63, no. 6, pp. 3479-3488, Jun. 2016.

[12] H. Jia, J. Wang, M. Cheng, W. Hua, C. Fang, and Z. Ling, “Comparison study of electromagnetic performance of bearingless flux-switching permanent-magnet motors,” *IEEE Trans. Appl. Supercond.*, vol. 26, no. 4, Jun. 2016, Art. ID. 5202305.

[13] T. Baumgartner and J. W. Kolar, “Multivariable state feedback control of a 500000-r/min self-bearing permanent-magnet motor,” *IEEE/ASME Trans. Mechatronics*, vol. 20, no.3, pp. 1149-1159, Jun. 2015.

[14] X. Sun, L. Chen, Z. Yang, and H. Zhu, "Analysis of inductance characteristics for a bearingless permanent magnet synchronous motor," *Electr. Eng.*, vol. 95, no. 3, pp. 277-286, Sep. 2013.

[15] X. Sun and H. Zhu, "Neuron PID control for a BPMSM based on RBF neural network on-line identification," *Asian J. Control*, vol. 15, no. 6, pp. 1772-1784, Nov. 2013.

[16] H. Sugimoto and A. Chiba, “Stability consideration of magnetic suspension in two-axis actively positioned bearingless motor with collocation problem,” *IEEE Trans. Ind. Appl.*, vol. 50, no. 1, pp. 338-345, Jan/Feb.2014.

[17] B. Lapotre, N. Takorabet, F. Meilbody-Tabar, R. Lateb, and J. Da Silva, “Radial force modeling for bearingless motors based on analyze of field origins,” *Proc. Inst. Mech. Eng. Part I-J Syst Control Eng.*, vol. 230, no. 4, pp. 311-319, Apr. 2016.

[18] B. M. Ebrahimi, M. J. Roshtkhari, J. Faiz, and S. V. Khatami, “Advanced Eccentricity Fault Recognition in Permanent Magnet Synchronous Motors Using Stator Current Signature Analysis,” *IEEE Trans. Ind. Electron.*, vol. 61, no. 4, pp. 2041-2052, Apr. 2014.